Engineering Structures 289 (2023) 116249

Contents lists available at ScienceDirect

Engineering Structures

journal homepage: www.elsevier.com/locate/engstruct

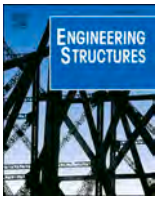

Additive manufactured Triply Periodical Minimal Surface lattice structures with modulated hybrid topology

Zhuo Xu [a], Irene La Mendola [b], Nima Razavi [a], Sara Bagherifard [b,*]

[a] Department of Mechanical and Industrial Engineering, Norwegian University of Science and Technology (NTNU), Trondheim, Norway
[b] Department of Mechanical Engineering, Politecnico di Milano, Milan, Italy

ARTICLE INFO

Keywords:
Lattice structures
Multi-morphology
Energy absorption
Fused deposition modeling

ABSTRACT

The fabrication freedom offered by additive manufacturing techniques is a unique asset to be exploited in the design of lightweight lattice structures. Adjusting topological and architectural features towards the design of multi-morphological lattice structures can offer a high potential towards obtaining fine-tuned mechanical response. Herein, to understand the role of unit cell topology and arrangement, various stacking and gradient strategies were implemented to modulate the overall mechanical response of the lattice structures under compression, using two Triply Periodical Minimal Surface (TPMS) unit cell designs. Experimental and numerical approaches were developed to reveal the deformation mechanism and failure modes and quantify stiffness, quasi-static uniaxial compressive strength, and energy absorption capacity of the structures. The topological arrangement of the selected unit cells was found to play a key role in defining the mechanical performance of the designed lattice structures. The obtained results demonstrated the high potential of various graded design elements for obtaining lattice structures with desired properties.

1. Introduction

The rapid advancement of additive manufacturing (AM) technologies has brought considerable attention to lightweight lattice or cellular structures. These structures generally consist of identical 3-dimensional unit cells arranged in a repeating and commonly regular array in space. In addition to their reduced weight, lattice structures can offer mechanical properties that may not be achievable in conventional solids. Studies have shown that changing architectural features in terms of unit cell size and shape, can offer a wealth of possibilities for tuning the deformation behavior and mechanical response of these structures for a wide range of applications [1–6] Among these, many studies have focused on enhancing the mechanical properties of cellular structures regarding stiffness, strength and energy absorption [7]. Changing the diameter of the struts at the junctions was found to considerably affect the static and fatigue response of cubic lattice structures [8]. Indeed, there has been a notable investment in functionally graded structures, where different topological features are modulated in a gradient manner [9,10]. Many studies have focused on the effect of graded volume fraction and porosity compared with homogeneous counterparts [6,11,12]. Different strategies have been implemented to adapt the density in functionally graded lattice structures [13,14]; these mainly include i) layer-wise adjustment of porosity by altering the strut diameter/thickness without changing the unit cell size or ii) varying the cell size using the same strut thickness/diameter. The effects of various gradient strategies including axial, dense-in, and dense-out were investigated numerically on the mechanical response of cubic and pillar octahedron-based lattice structures at overall porosities of 60%, 75%, and 85%. The functionally graded structures exhibited structural collapse starting from the lower density layers, regardless of the unit cell type. Power-law analysis based on the Gibson-Ashby model [15] confirmed the stretch-dominated behavior of the cubic structures and the bending-dominated response of pillar octahedron structures under quasi-static compression, irrespective of the implemented gradient strategy [16].

In addition to changing strut thickness or unit cell size, using hybrid lattice structures made of unit cells of different topologies within the same structure can bring another level of tunability to lattice structures. The rationale behind defining hybrid lattice is to take advantage of the strengths of each unit cell toward an even further enhanced mechanical performance through local control of deformation modes in the structure. For instance, inspired by metallurgical concepts, many studies

* Corresponding author.
E-mail address: sara.bagherifard@polimi.it (S. Bagherifard).

https://doi.org/10.1016/j.engstruct.2023.116249
Received 22 February 2023; Received in revised form 31 March 2023; Accepted 29 April 2023
Available online 12 May 2023
0141-0296/© 2023 The Authors. Published by Elsevier Ltd. This is an open access article under the CC BY-NC-ND license (http://creativecommons.org/licenses/by-nc-nd/4.0/).

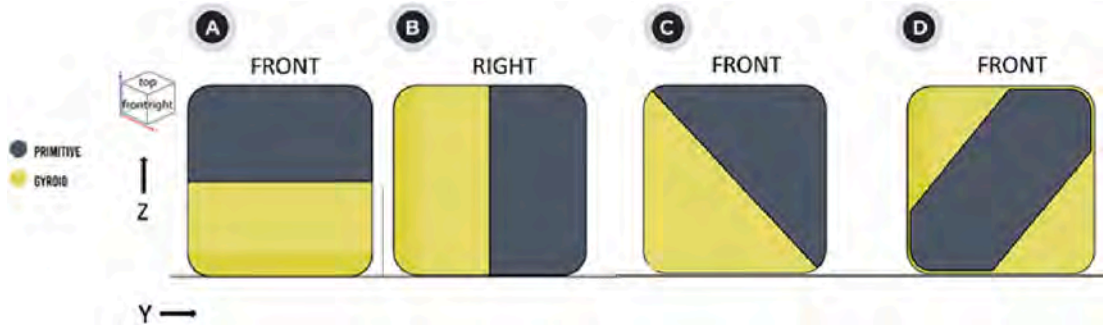

Fig. 1. Schematic illustration of the defined hybrid multi-morphology structures: A) linear transition along the loading direction, B) linear transition perpendicular to the loading direction C) diagonal transition, D) localized diagonal transition.

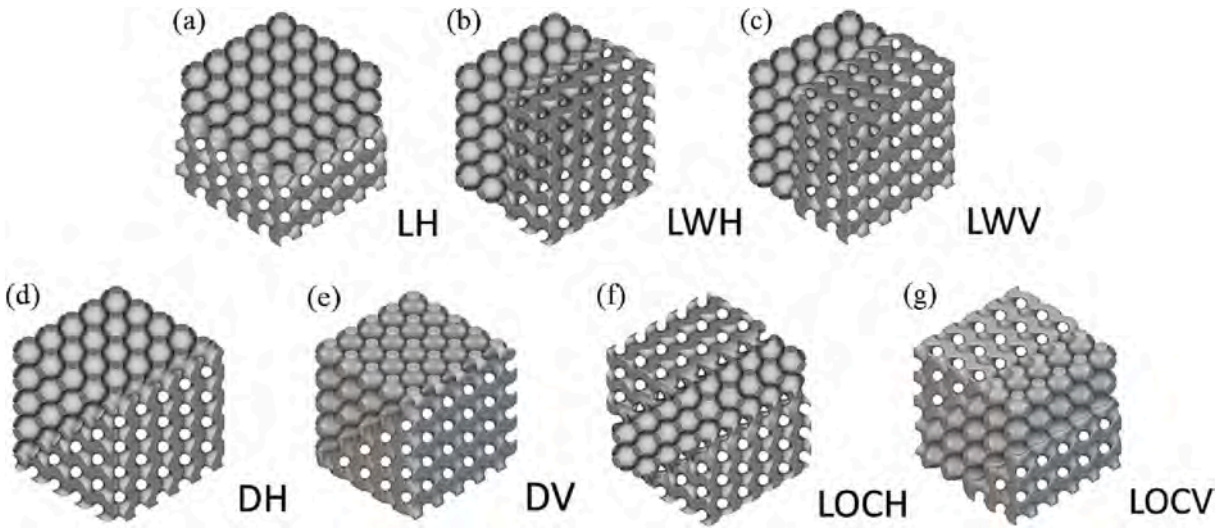

Fig. 2. Design of multi-morphology structures via linear transition: a) along height (LH), b) along width through horizontal waves (LWH) and c) along width through vertical waves (LWV). Design of multi-morphology structures via diagonal transition: d) through horizontal waves (DH), e) through vertical waves (DV). Generation of multi-morphology structures via localized diagonal transition: f) through horizontal waves (LOCH), and g) through vertical waves (LOCV).

investigated the combinations of body-centered cubic (BCC), and face-centered cubic (FCC) unit cells in lattice structures. This approach was used to mimic the hardening mechanisms of crystalline materials including grain boundaries, precipitates, and phases to obtain robust and damage-tolerant lattice structures [17]. Combination of FCC and BCC lattice was also reported to enhance plastic energy absorption [18] and promote controlled anisotropy [19]. Multi-morphology structures were made of two materials of different properties to also investigate the interplay of base material properties within the hybrid topology. The results indicated that the architecturally hybrid materials could highly enhance energy-absorption capacity, leading to higher performance compared to both homogeneous lattice structures and predictions of rule-of-mixtures [18]. Combination of auxetic and hexagonal honeycomb unit cells was used in another study to improve energy absorption properties of lattice structures, by promoting a uniform and stable deformation behavior [20]. Auxetic behavior refers to exhibiting negative Poisson's ratio [21]. In this study, the geometrical parameters of the unit cell walls were adjusted to further alter the load bearing and energy absorption capacity of the structures [20]. In another study, four-unit cell topologies of BCC, FCC, together with new designs based on the combination of BCC with FCC, and combination of BCC, FCC, and vertex cube were regularly arranged in space following horizontal, vertical, and circular patterns. The results indicated the prominent effect of arrangement and unit cell geometry on the strength of the lattice structure and their failure mode, with layer-by-layer failure identified as the dominant mode for horizontal hybrid structures and shear failure for vertical and circular structures [2]. Failure mode of different strut-based unit cell topologies (Octet truss, Rhoctet and Rhoctan) stacked in alternating rows loaded under different loading directions and strain rates were reported to change in response to higher strain rate. Compression tests highlighted the effect of the stacking direction and architectural order on the response of the structure revealing that in most cases the weakest topology determined the mechanical strength of the hybrid structure [4].

Despite the progress in the design and fabrication of hybrid lattice structures, there are still several knowledge gaps on the role of gradient strategy, loading direction, and topological combinations on the global mechanical performance of these hybrid structures. Here we analyzed the role of gradient topology on load-bearing characteristics of lattice structures to understand how the topology and stacking strategy of the constituent unit cells can modulate the overall mechanical response. Two well-known unit cells from the family of triply periodical minimal surface (TPMS) unit cells have been selected to take advantage of their distinct qualities. TPMS designs are nodal-based hyperbolic smooth surfaces in nature and thus are characterized with reduced stress localization. Here we selected Gyroid and Schwarz primitive designs as representative bending- and stretch-dominated TPMS unit cells. The popularity of Gyroid structure is due to the characteristics of easy manufacturability, high porosity, excellent cell growth and migration in biomedical applications [22]. It is acknowledged that Gyroid structure under compression generally involves a failure typical of brittle materials [23] due to the tendency of bending deformation according to the

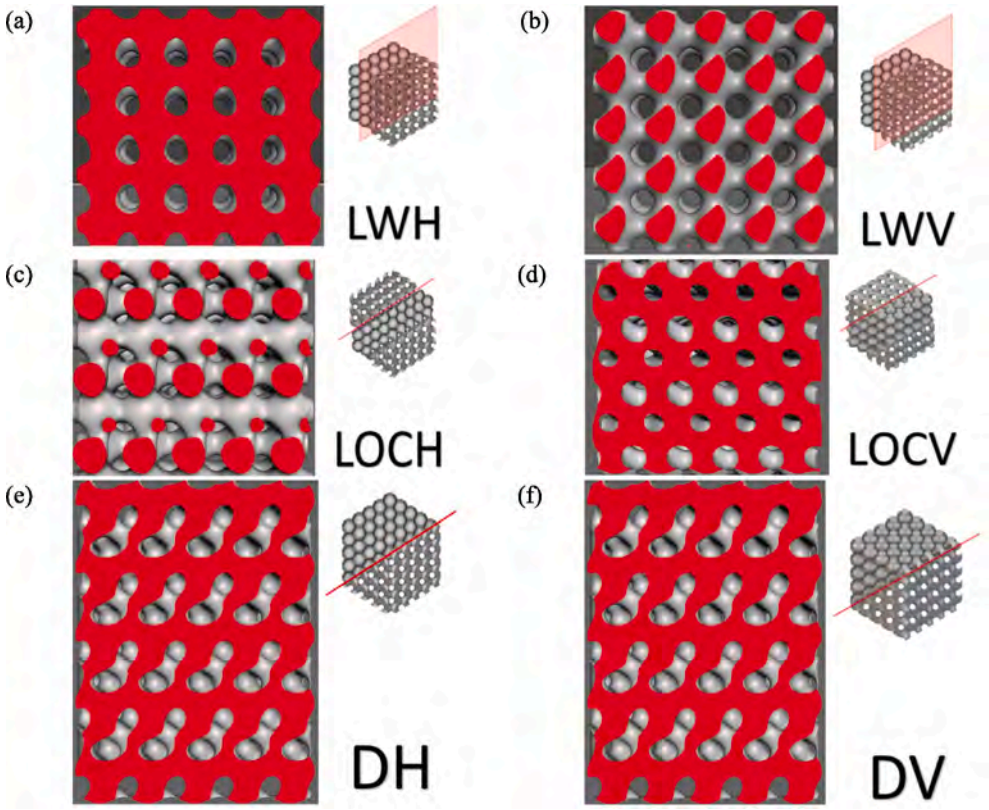

Fig. 3. Contact morphology of interface (marked in red) between Gyroid and primitive structures for different lattice geometries including (a) LWH (b) LWV (c) LOCH (d) LOCV (e) DH (f) DV. (For interpretation of the references to colour in this figure legend, the reader is referred to the web version of this article.)

Table 1
Process parameters for fabricating the lattice structures.

Building parameters	Parameter value	Building parameters	Parameter value
Layer height	0.1 mm	Build plate temperature	75 °C
Initial layer printing speed	30 mm/s	Printing speed	45 mm/s
Contour thickness	0.8 mm	Raster angles	±45 degrees
Contour line count	2	Nozzle diameter	0.4 mm
Infill density	100%	Nozzle temperature	215 °C
Retraction distance	35 mm	Retraction speed	0.5 mm/s

Table 2
Tensile properties of ASTM D638 Type II dogbone specimens with a thickness of 3 mm.

Property	Test1	Test2	Test3	Test4	Results
σ_u (MPa)	57.18	57.21	56.76	56.16	56.83 ± 0.49
σ y (MPa)	53.41	52.61	51.98	52.11	52.53 ± 0.65
ε %	2.63	2.66	2.53	2.66	2.62 ± 0.06
ν	0.34	0.38	0.35	0.36	0.36 ± 0.02
E (GPa)	3.12	3.14	3.04	3.16	3.12 ± 0.05

theories of Ashby and Gibson. Therefore, to enhance the compression resistance of the lattice Gyroid -based structures, hybrid structures were designed with the combination of Gyroid and Schwarz primitive unit cells. The idea is to combine all the advantageous behavioral characteristics of these cell structures and enhance their mechanical properties compared to uniform designs, by attempting to interrupt or deflect premature crack propagation.

Numerical and experimental analyses were performed to investigate the effect of various arrangements (uniform, linear transition along height, linear transition along width, diagonal transition and diagonal local transition) on structures' mechanical response under compressive loading. In each strategy, two options of transition through horizontal and vertical waves were considered for the Gyroid unit cell. Experimental and numerical results have been discussed in detail in terms of stiffness, quasi-static uniaxial compressive strength, and energy absorption capacity. The results indicated the possibility to modulate the overall mechanical response by adjusting the arrangement of the unit cells and thus controlling the formation of localized bands of high stress and mechanical collapse under compression. Finite element analysis of the structures revealed the deformation mechanism and failure modes. The topological arrangement of the selected TPMS unit cells was found to play a key role in defining the energy-absorption performance of the designed lattice structures.

2. Materials and methods

nTopology (nTopology lnc, USA) was selected as the software to generate the functionally graded lattice structures. This 3D modeler is based on implicit modeling, which offers the possibility of creating complex lattice structures. The dimensions of the lattice structures were determined to be 30 × 30 × 30 mm with five unit cells along each side. The dimensions of the lattice structures such as overall cube dimension and unit cell size were determined based on the manufacturing constrains such as fabrication time, fabrication quality, and size limitation imposed by the testing machine. There is a trade-off between the number of unit cells and the size of unit cells. The boundary effect will be more dominant if within the same cube size, the number of the unit cells is smaller. On the contrary, for a higher number of unit cells in the same cube size, the design features become smaller which can directly influence the quality and geometrical accuracy of the printed parts using FDM printer. Relative density in the designs was set to be constant,

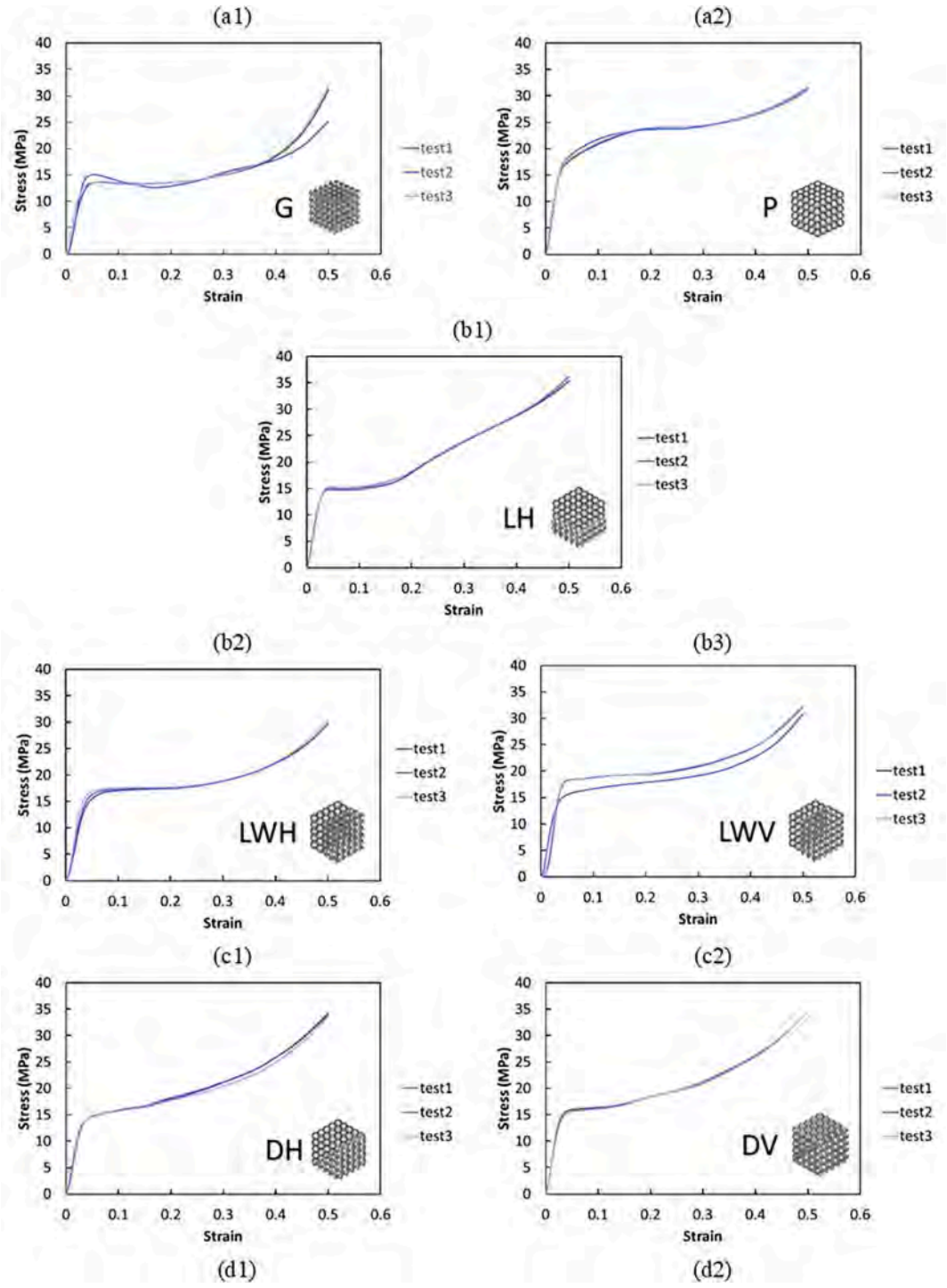

Fig. 4. Stress–strain curves of compression tests for uniform lattice structures of (a1): G, (a2) P, linear transition of (b1): LH, (b2): LWH, (b3): LWV, diagonal transition of (c1): DH, (c2): DV and localized diagonal transition of (d1): LOCH, (d2): LOCV.

approximately 50% of the volume fraction regardless of the unit cell types.

2.1. Topological design

Different categories of structures composed of Gyroid and Schwarz primitive unit cells were hypothesized distinguished by the direction or topology of the cells. Within each macro-category, three transition strategies were identified as opposed to the reference uniform structures, including linear transition, diagonal transition, and localized diagonal transition. These categories are schematically presented in Fig. 1. Within these categories we have considered unit cell type linear transition parallel to the loading direction (along the height of the structure, see Fig. 1**A**), in the direction perpendicular to the loading direction, thus along the width of the structure (see Fig. 1**B**) and diagonal transition (Fig. 1**C**). In the case of local diagonal transition (see Fig. 1**D**), the design objective is to modify the behavior of the uniform Gyroid lattice that by nature commonly collapses through a diagonal shear band [24]. These bands are reported to appear at a specific angle from the loading direction [24]. The arrangement of the transition area

Table 3
Mechanical properties of different lattice structures.

	Geometries	E [MPa]	Yield Stress [MPa]	FPS [MPa]	Wv [J/mm^3]
Uniform	G	500.5(±21.3)	9.5(±2.4)	13.9(±0.8)	2.9(±0.3)
	P	698.0(±19.2)	14.1(±0.8)	16.6(±1.9)	6.4(±0.1)
Linear transition	LH	600.3(±47.5)	10.5(±1.9)	14.7(±0.2)	1.6(±0.2)
	LWH	518.0(±61.9)	11.3(±0.4)	15.9(±0.3)	4.1(±0.1)
	LWV	682.1(±10.4)	12.9(±1.1)	17.3(±0.2)	4.8(±0.3)
Diagonal transition	DH	540.9(±16.9)	10.6(±0.7)	15.1(±1.5)	2.1(±0.1)
	DV	612.3(±19.6)	12.7(±0.5)	15.4(±0.4)	1.9(±0.1)
Localized diagonal transition	LOCH	549.0(±55.8)	13.8(±5.5)	13.9(±0.4)	2.6(±0.1)
	LOCV	512.0(±27.4)	10.6(±2.4)	13.7(±1.9)	3.4(±0.8)

in the diagonal transition design is along the same angles with respect to the loading direction.

The deformation behavior of these structures was analyzed considering different configurations of Gyroid unit cells. Two different configurations with zero and half unit cell shift along the depth were considered when constructing the Gyroid part of the structure, resulting in horizontal or vertical waves of the Gyroid part on the sample surface, in order to determine the sensitivity of the mechanical response to this local orientation. In the structure for which transition occurs along the width (Fig. 1**B**), both horizontal and vertical waves of the Gyroid unit cells are displayed on the same structure parallel to the loading direction (see Fig. 2**b and c**). For brevity, this variation is not shown in Fig. 2 for all designs.

In the design of hybrid structures, the most critical site is the interaction zone between dissimilar unit cell geometries, which can cause a stress peak due to the sudden change of topological features [25]. To minimize this, the transition zone should be continuous and linear without abrupt changes or containing sharp angles at the interfaces. Thus, appropriate strategies were implemented in the geometrical design to develop a continuous morphological transition and control the smoothness of the morphological transition in nTopology. Fig. 2 illustrates the designs of different models.

The geometries were defined to follow the Design for Additive Manufacturing (DfAM) principles to avoid complications during fabrication that was planned through Fused Deposition Modeling (FDM) printing. This includes considering self-supporting structures with adequate thicknesses and shapes to ensure the fabrication feasibility of the high-quality components. Another important aspect is that the orientation of the Gyroid waves, regardless of the definition of the geometries based on the direction of the Gyroid waves (horizontal or vertical) on the outer faces, can vary deep inside the structure due to the periodicity of the unit cells. Therefore, the morphology on the faces where Gyroid and primitive units meet can vary at different cross sections. For instance, when considering the horizontal direction for the waves, the primitive unit cells are in contact with the entire basic Gyroid unit cells (For instance, see Fig. 3**(a)**). While the primitive unit cells will be in contact with half-shifted Gyroid unit cells in the direction of vertical waves, which results in a different interface morphology (For instance, see Fig. 3**(a) and 3(b)**). Possible contact faces are illustrated in Fig. 3. Therefore, it is also essential to study how different contact morphologies can influence the mechanical properties under quasi-static compression.

2.2. Specimen fabrication and experimental tests

The test specimens were fabricated via FDM technique using Original Prusa i3 MK3 with PLA filament (3DNet, Norway) of 1.75 mm diameter. The process parameters are shown in Table 1. Besides lattice specimens for compression test, tensile specimens were designed (Type II ASTM D638) and fabricated with similar process parameters as the lattice samples and tested using MTS Criterion model C42 electromechanical load frame with a load cell capacity of 5 kN at a crosshead speed of 2 mm/min. The tensile properties including ultimate tensile stress (σ_u), yield stress (σ_y), elongation at failure (ε), Poisson's ratio (ν), and Young's modulus (E) of the fabricated PLA samples are listed in Table 2.

The purpose of the experimental analysis is to evaluate the mechanical performance influenced by the geometry, as well as the reproducibility of the structures fabricated via the FDM technique. All the lattice structures were tested under quasi-static compression using an electromechanical MTS Alliance RF150 machine with a maximum 150 kN load cell. The compression rate was set to be 2 mm/min and the ultimate compression strain was approximately 50% of the original height. A fixed camera system was employed to capture high-resolution images with a pre-defined sampling frequency during the compression tests. Compression load and displacement data were collected to calculate the stress dividing the compression load by the effective area of the contact surface i.e., actual surface area multiplied by the percentage of relative density due to the uniformity of relative density in all lattice structures) and engineering strain (actual displacement divided by the original height of the lattice). Mechanical properties were analyzed regarding stiffness in compression (E_{latt}), Yield stress (σ_y), Peak stress (F_{PS}), Energy absorption per unit volume (W_v) and Energy absorption per unit mass (W_m).

It is worth mentioning that all the values of energy absorption per unit volume and per unit mass were calculated based on the compressive strain ranging from 0 to 50%.

Since local plasticity may occur in the structure at stresses well below the general yield of the structure [26], the stiffness was obtained from the gradient value of the trend line given by linear fitting of data points within the elastic stage at the beginning of the compressive stress–strain curves. ASTM D638 standard suggests excluding early points where the system has yet to stabilize producing a curve with a different trend [27]. Accordingly, stiffness was calculated in the linear elastic region after elimination of unstable initial points, considering linear regression model R^2. Yield stress was derived from the intersection between the compressive stress–strain curve and the 0.2% offset line parallel to the elastic region. The first peak stress was estimated as the compressive stress corresponding to the first local stress prior to a change in the trend of the stress–strain curve passing from the elastic region to the plateau area. Finally, the energy absorption values prior to the densification stage of the structure were obtained by calculating the area under the stress–strain curve.

2.3. Numerical simulations

In the simulations, the compression behavior was simulated up to 30% of the strain using Abaqus 2017 for some of the lattice structures to analyze the local deformation and failure mechanism and accurately determine the stress concentration sites. Two uniform Gyroid and Schwarz primitive structures as well as other four hybrid structures including LH, LWV, DV, and LOCV were analyzed numerically and compared with the corresponding experimental results, to check the effect of morphological characteristics and the relationship between building and load direction. Specifically, stiffness and yield stress were obtained from the numerical simulation and compared with the experimental data.

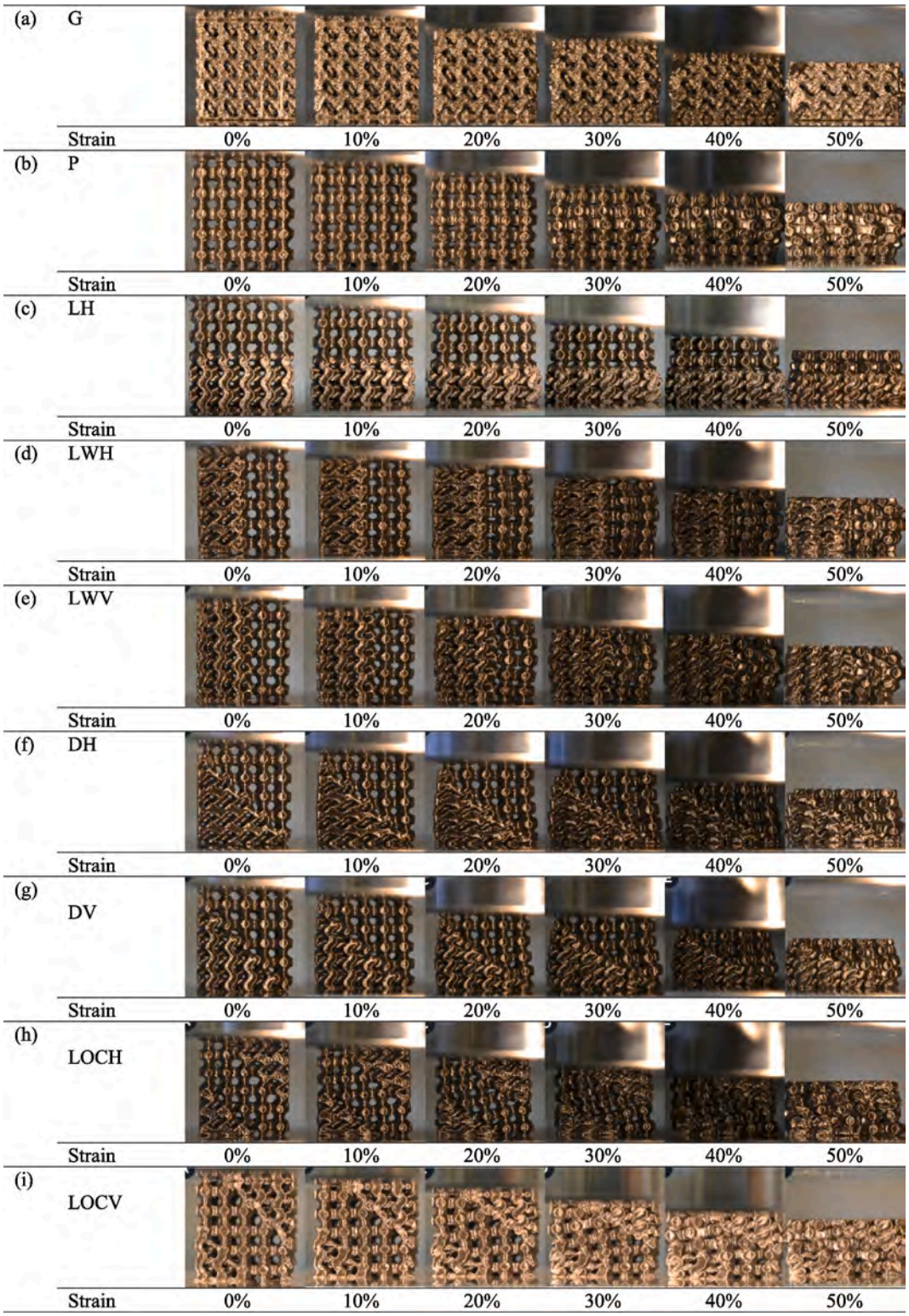

Fig. 5. Snapshots showing the deformation of different lattice structures for (a): G, (b): P, (c) LH, (d), LWH, (e) LWV, (f) DH, (g), DV, (h) LOCH, (i) LOCV, from 0% to 50% compressive strain.

The geometries were imported into Abaqus and meshed using quadratic meshing type. A constant vertical velocity was applied to the upper face of the lattice structure while all the degrees of freedom were restrained on the bottom face. An elastic perfectly plastic material model was defined according to the experimental tensile tests performed on dog-bone specimens (See Table 2). Computational time is one of the most concerning aspects of numerical simulation, specifically affected by mesh size and step time. To reduce the computational time here, time scaling approach was implemented to simulate the quasi-static compression condition. Special attention was made for the use of time scaling as this parameter is related to the wave propagation speed in the elements, which is directly related to the density of the material and

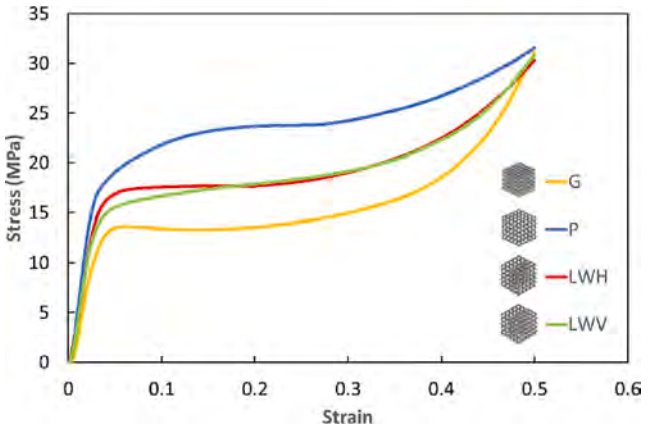

Fig. 6. Comparisons of stress–strain curves between 'G', 'P', 'LWH' and 'LWV' lattice structures.

element size. According to the literature studies, the kinetic energy of the system must not exceed 10% of its internal energy during the process in a quasi-static analysis [28]. Several trials were made to minimize the adverse effects by comparing the stiffness and the curve trend mainly in the elastic zone with those obtained from the experimental analysis of the same structure. The loading velocity of 400 mm/s was found to offer a good balance between processing time and the results' quality without interfering with the ratio between kinetic and internal energy. A mesh size of 0.5 mm was considered after mesh convergence analysis. Two rigid surface planes were defined on the top and bottom planes to which the velocity and encastre constraints were applied. For comparing the numerical data with experiments, the mean stress–strain curve obtained from three experimental replications performed of each geometry was considered. It can be observed that the discrepancy between each curve is very small from the presented stress–strain curves. For obtaining the mean stress–strain curve, the stress values were averaged per specific strains.

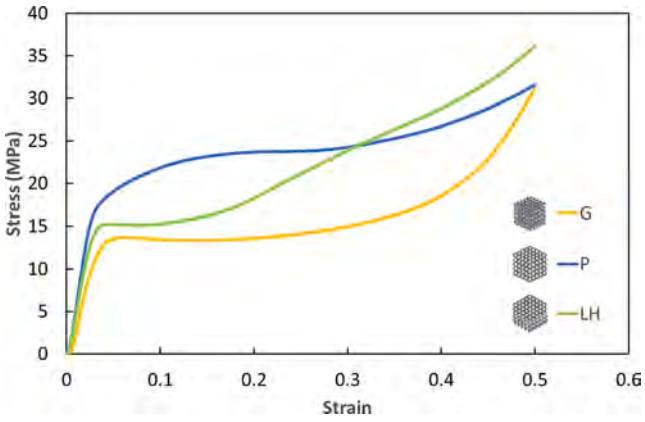

Fig. 8. Comparisons of stress–strain curves between G, P, and LH lattice structures.

3. Results and discussion

3.1. Experimental results

The representative stress–strain curves obtained from the compression tests on lattice structures are illustrated in Fig. 4 including four categories of uniform, linear transition, diagonal transition, and localized diagonal transition. The typical shape of the graphs includes an elastic region up to the yield point and the first peak, followed by the variation of the trend, which identifies a plateau area, continuing up to the densification stage. Overall, it can be observed that all the tests exhibited a good level of consistency and reproducibility of the lattice structures as illustrated in Fig. 4. The detailed extracted mechanical properties are reported in Table 3. The snapshots in Fig. 5 presenting the deformed shape of those lattice structures in a strain range of 0 to 50%.

3.1.1. Design-specific mechanical properties

In the case of the uniform Gyroid structure (G), as shown in Fig. 5**(a)**, the second layer from the bottom started to deform at around 10%

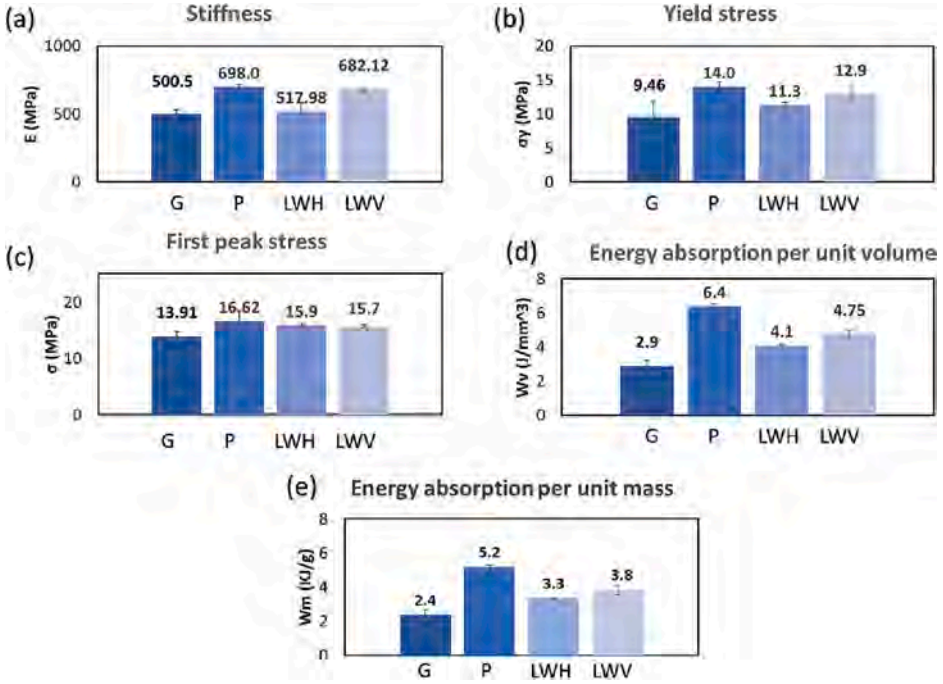

Fig. 7. Bar charts representing comparisons of the mechanical properties of P, G, LWH and LWV. a) Stiffness, b) yield stress, c) first peak stress, d) energy absorption per unit volume, (e) energy absorption per unit mass.

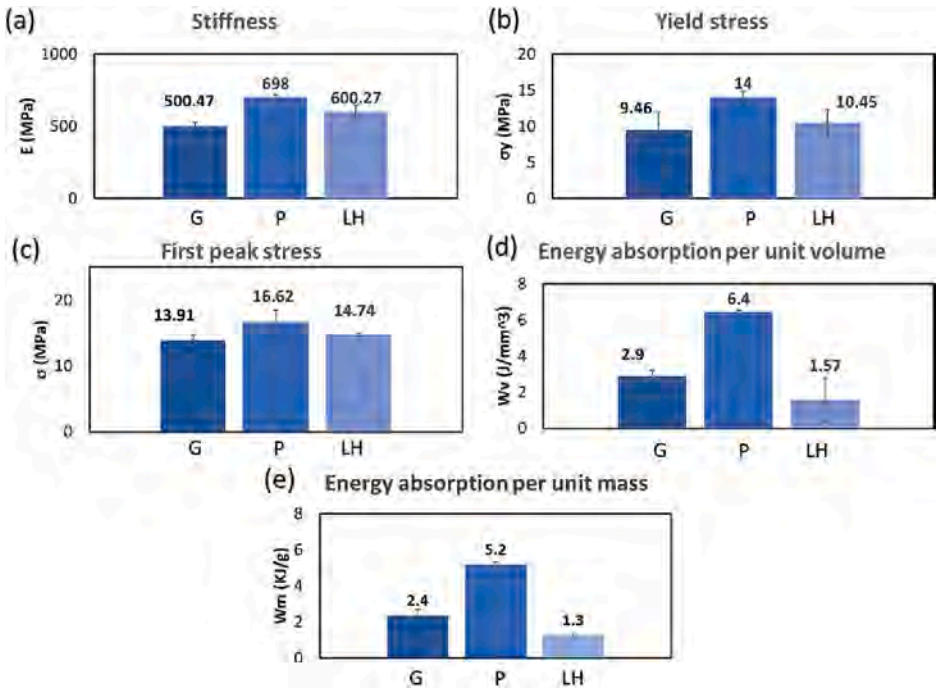

Fig. 9. Bar charts representing comparisons of the mechanical properties of P, G and LH structures: a) Stiffness, b) yield stress, c) first peak stress, and d) energy absorption per unit volume, (e) energy absorption per unit mass.

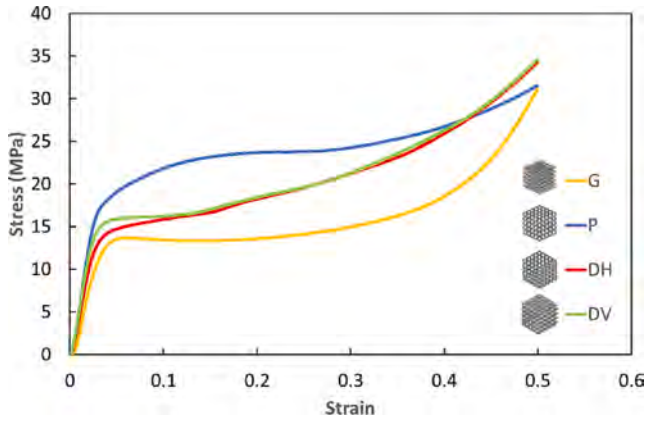

Fig. 10. Comparisons of stress–strain curves between G, P, DH and DV lattice structures.

strain. Subsequently, the failure transferred to the adjacent third layer at around 20% strain, followed by the fourth layer collapsing until densification with a rapid increase of stress at around 25% strain. Once the local densification was observed, the structure continued to be compressed up to 50% through the collapse of the fifth layer at around 40% strain. It is worth mentioning that local densification refers to the deformation behavior in which certain areas of the lattice experience a higher degree of compression or deformation compared to other areas, especially when the structure experiences non-uniform deformation under compression. The stress–strain curve corresponding to this sample exhibited a large and stable plateau area that affects the energy absorption capacity (see Fig. 4**(a1)**).

Regarding the uniform primitive structures (P), the compression of the struts occurred initially in a uniform way for all layers up to around 10% strain as illustrated in Fig. 5**(b)**. Then the unit cells in the middle row of the structure (i.e., third layer from the bottom) started to deform leading to outwards sliding. This deformation was followed in the adjacent layers until 30% strain when the three middle layers were in contact. Ultimately, the local densification occurred for the second, third and the fourth layers prior to 50% strain while the other struts were experiencing only symmetric deformation. In this case, the stress increment was relatively lower in comparison with the uniform Gyroid structure (see Fig. 4**(a1)** and **4(a2)**). Unlike the uniform Gyroid (G) structure, the uniform primitive (P) structures are classified as stretch-dominated instead of bending-dominated, thus with a tendency for strut buckling followed by a layer-by-layer consecutive failure mechanism.

As for the Gyroid lattice structures with transition along with height under the linear transition category (LH), it began to deform from the interface layer at around 10% compression strain as illustrated in Fig. 5 **(c)**. Between 10% and 20% strain, the interface collapsed on the adjacent layer below and the failure of the interface layer occurred vertically instead of horizontally. The main deformation occurred in the Gyroid part and caused uniform deformation prior to the densification point at around 30% strain. This compression behavior agrees with the results reported in other studies [6,28]. Once the Gyroid part of the structure experienced complete uniform compression, the deformation continued along the struts of the primitive structures starting with the fourth layer and then propagated to the fifth layer. In this case, there was a slight horizontal slip of the struts that occurred on the fourth layer of the primitive part. The deformation of the primitive part occurred after the densification stage of the Gyroid part, which indicates the higher load-bearing capability for the primitive zone, as also confirmed in Table 3 for uniform structures.

Next is the Gyroid structures with transition along width under the same category (LWH), in which the building direction is transverse to the loading direction while the interface is perpendicular to the loading direction. In this case, the compression behavior was partially bending-dominated and partially stretch-dominated. Overall, a global uniform failure pattern was observed during the compression test (see Fig. 5**(d)**). At first, the primitive part of the structure (the right side of the lattice structure) began to experience uniform deformation. Then the middle layer started to deform outwards horizontally followed by the adjacent layers' deformation at around 20% strain. As for the other half portion of the Gyroid structures, it did not buckle but the bending of the struts led

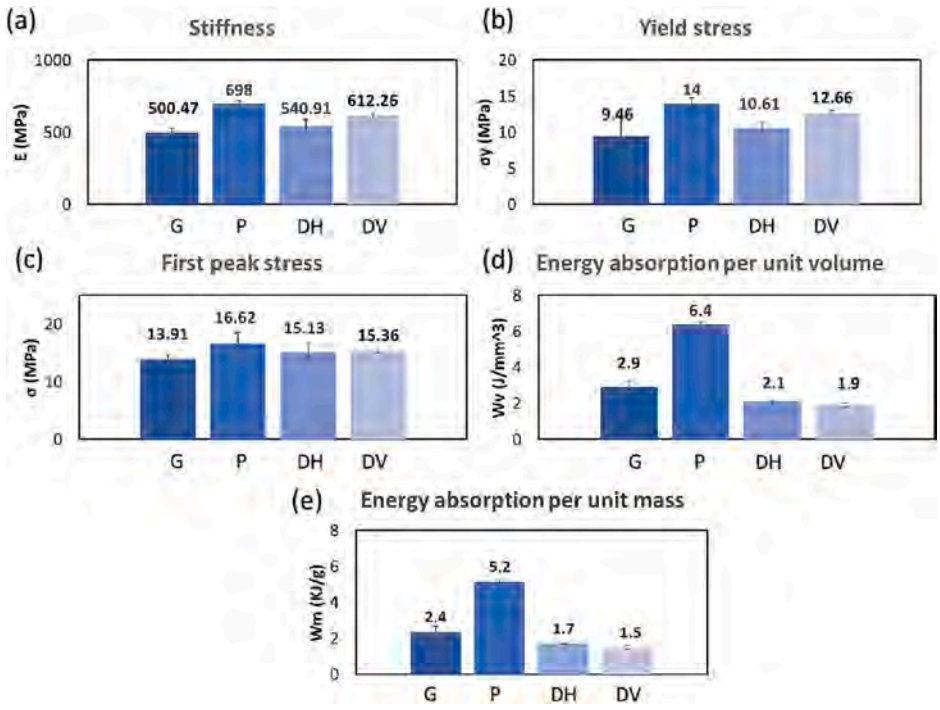

Fig. 11. Bar charts representing comparisons of the mechanical properties of P, G, DH and DV structures. a) Stiffness, b) yield stress, c) first peak stress, d) energy absorption per unit volume, (e) energy absorption per unit mass.

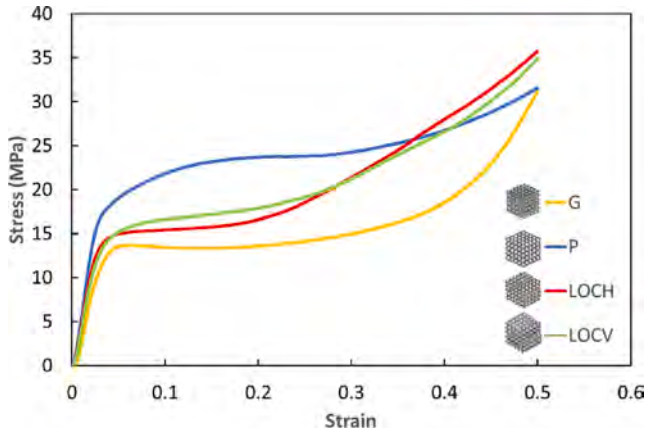

Fig. 12. Comparisons of stress–strain curves between G, P, LOCH and LOCV lattice structures.

to progressive fracture and started the densification phase shortly after 25% strain. The stress–strain curve for LWH demonstrated a longer and smooth plateau area that ended at 25% strain with higher energy absorption than LH before densification as illustrated in Fig. 4 **(b2)** and listed in Table 3.

Similar compressive behavior was observed for the structure with transition along the vertical lines of the Gyroid (LWV) as illustrated in Fig. 5**(e)**. It is worth mentioning that the vertical waves feature only occur on the outer faces of the sample and the dominant part of the structure that affects the mechanical properties is the connecting interface as previously demonstrated in Fig. 3**(b).** Therefore, it can be observed that the average values of all the mechanical properties for LWV are slightly higher than those of LWH as reported in Table 3.

After the category of linear transition, two structures that exhibit variation along the diagonal of the specimen (45 degrees to the loading direction) were analyzed. The first case was with diagonal transition through Gyroid horizontal waves (DH), in which the deformation initiated on the transition area at the strain of 10% as illustrated in Fig. 5 **(f).** The structure started to deform involving strut bending of the Gyroid part and outward deformation of the primitive part from the contact zone with the downward interface. At 10% strain, the interface transmitted the total load towards the Gyroid part shortly after the densification point, exhibiting a short plateau area but with a gradual increase of the stress as well as the increase in energy absorption capacity. The adjacent unit cells were affected by the deformation due to the collapse along the diagonal of the structure. At around 30% strain, the deformation was observed in the Gyroid part and the contact point with the interface to the top of the structure. The Gyroid unit cells experienced the same compression behavior but in the opposite direction with strut bending and structural collapse.

Similarly, almost identical compression behavior at different stages of the strain was observed for the structure with vertical Gyroid waves along the diagonal on the surface (DV). The contact morphology of the interface for DH and DV are identical as illustrated in Fig. 3**(c)** and Fig. 3 **(d)**. Therefore, the wave direction for the Gyroid part of the structure on the surface is the only structural difference between these two designs. Based on the experimental results reported in Table 3, the yield stress, first peak stress and energy absorption are very close for these two structures except for the slightly higher stiffness of DV compared to DH.

Dealing with specimens with localized diagonal transition via horizontal waves (LOCH) (see Fig. 5**(h)**, there is an initial deformation in the two transition areas that began to slip horizontally at 20% strain. The lower load-bearing capacity of the Gyroid part compared to the primitive part, led to uniform deformation of the hybrid structure. The load transmission in the primitive part occurred gradually from the two transition zones toward the inside. The unit cells on the bottom part of the structure experienced bending with the horizontal slipping of the struts, while the top part was compressed with a slight buckling and then collapsed along the struts. The primitive part of the structure reached the densification point at around 40% strain, which indicates that the primitive structure is more compression resistant compared to the Gyroid structure with the densification stage occurring at around 20% strain. When referring to the structure with localized diagonal transition via vertical waves (LOCV) as illustrated in Fig. 5**(i)**, similar compression

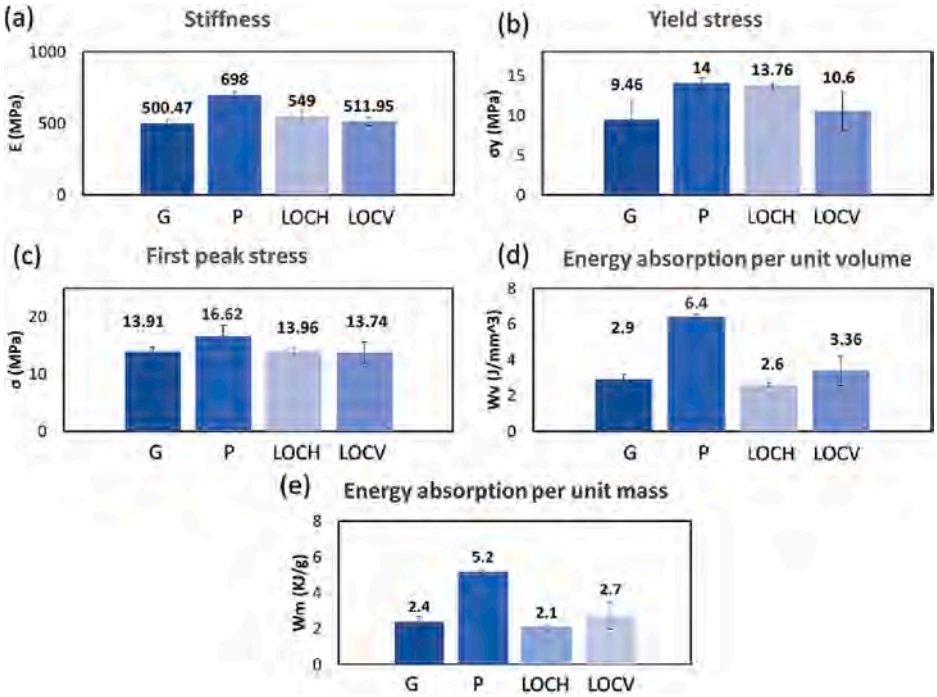

Fig. 13. Bar charts representing a comparison of the mechanical properties of G, P, LOCH and LOCV structure: a) Yield stress, b) stiffness, c) first peak stress, d) energy absorption per unit volume, (e) energy absorption per unit mass.

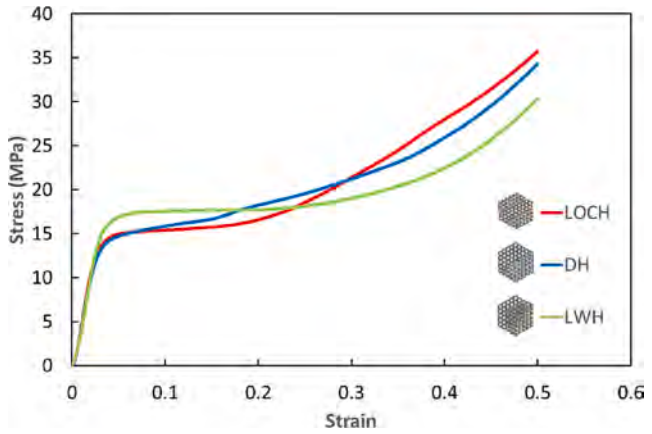

Fig. 14. Comparisons of stress–strain curves between LOCH, DH and LWH lattice structures.

behavior was observed for the strain range from zero to 50%. However, one difference is that the vertical struts on the surface of LOCV structure experienced bending and cracking while the horizontal waves within the Gyroid part did not exhibit such failure modes since the direction of the waves was perpendicular to the loading direction. Therefore, the stiffness of LOCV was slightly lower than LOCH, as reported in Table 3.

3.1.2. *Comparing different transition strategies*

To assess whether it is possible to take advantage of the hybrid structures compared to the classical uniform morphologies, a comparative discussion for each transition type is provided in this section. Generating a diagram that reports all the properties of different structures is not very perceptive when there are various parameters changing between different structures in addition to morphologies, including the orientation of the features with respect to the loading directions. Therefore, two categories including transition type and orientation of surface waves with respect to the loading direction will be analyzed and discussed. Specifically, there are four different transition types including i) linear transition along the width, ii) linear transition along with the height, iii) diagonal transition, and iv) localized diagonal transition in the first category, and the second category is comprised on two groups with a) Gyroid horizontal waves and b) Gyroid vertical waves on the sample surface. Representative stress–strain curves for each group were selected for comparison.

For the linear transition along width category, four geometries including G, P, LWH, and LWV were compared as illustrated in Fig. 6. The geometries of LWH and LWV structures demonstrated a very similar behavior except for a slightly higher peak stress at an equal plateau area exhibited by LWH structure. In addition, the curves of LWH and LWV structures are in between the two uniform structures, indicating that the hybrid structures show a modulable response between the stretching and bending-dominated behaviors. Both LWH and LWV structures displayed higher load-bearing capacities than the G structure, but lower values compared to the P structure. In addition, both LWH and LWV structures contain smoother and more extended plateau areas compared to the G structure even if followed by a slightly increasing trend. As for the comparison of deformation mechanisms between each structure, it can be discovered that except for G structure, the barrel shape occurred for the P, LWH and LWV structures at around 20% of the strain, which is in the plateau area of the curves. This is an indication that P, LWH and LWV structures experienced uniform deformation under compression.

When referring to the mechanical properties of these structures in Fig. 7, it can be observed that LWV structure has higher yield stress than LWH structure and lower yield stress compared to the P structure while its stiffness is just lower than that of the P structure. This hybrid design provides a structure stiffer and stronger compared to other cases except for P, and according to the value derived from the plateau area extending up to 28%, it also has higher energy absorption capacity compared to the uniform Gyroid and LWH structures. The LWH structure, on the other hand, has higher peak stress and stiffness than the G structure but lower energy absorption with respect to the LWV structure, despite exhibiting a good energy absorption prior to entering the densification at about 26% strain.

As for the linear transition along the height (LH), the effect of linear

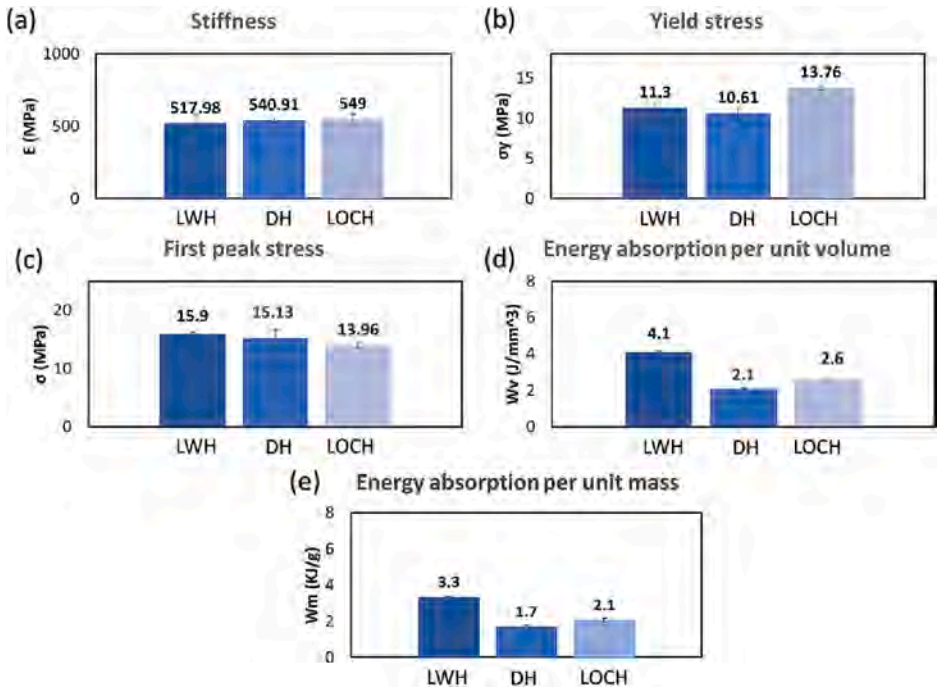

Fig. 15. Bar charts representing comparisons of the mechanical properties of LOCH, DH, and LWH structures: a) Stiffness, b) yield stress, c) first peak stress, d) energy absorption per unit volume, (e) energy absorption per unit mass.

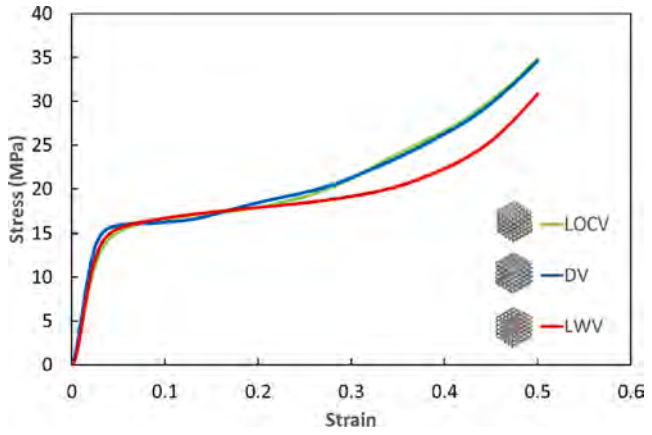

Fig. 16. Comparisons of stress–strain curves between DV, LWV and LOCV lattice structures.

transition of unit cell types was compared with the two corresponding uniform structures in Figs. 8 and 9. Fig. 8 illustrates a higher stiffness and compression resistance of the hybrid LH structure compared to the G structure, whereas compared to the P structure it shows lower stiffness and compression resistance. However, the LH structure represents a significantly shorter plateau region compared to the two uniform structures, which significantly reduces the ability for absorbing energy under compression as illustrated in Fig. 9. One of the primary reasons can be attributed to the interface characteristics of the LH structure compared to the rest of the samples. It was also observed that the deformation of the LH structure started at the interface in the middle and then extended in the struts of the G part of the structure that experienced bending and a complete densification as illustrated in Fig. 5**(c)**. A relatively uniform deformation in the P part of the structure occurred after the progressive collapse of the less resistant part of the structure at an early stage of the densification process. In this case, the energy absorption was only considered prior to the densification of the Primitive part of the structure. On the contrary, the yield stress of LH structure is between G and P structures as well as its first peak stress.

A comparative illustration of stress–strain curves obtained from specimens of four geometries including G, P, DH and DV, all under the category of diagonal transition strategy, is shown in Fig. 10. As previously described, the deformation started at the interface for both DH and DV structures. However, the horizontal waves of the DH structure did not experience fracture but only strut barreling and buckling (see Fig. 5 **(f)**) while in the DV structure the vertical waves of the G part presented some cracks with the formation of shear bands (see Fig. 5**(g)**). The DV structure demonstrated a higher stiffness and yield stress compared to the DH one; but almost equal values for first peak stress and energy absorption were obtained. This observation can be attributed to the identical connection interfaces in both DH and DV structures. Therefore, the only difference between these two structures is the direction of the waves on the surface, which is the sole factor that can cause variation in the mechanical properties. G structure reached the densification stage at around 20% strain, which indicates that the plateau area is larger than the other two hybrid curves but smaller than that of the P structures. In addition, the DH structure exhibited similar mechanical properties to the G structure as illustrated in graphs of Fig. 11. In contrast, the DV structure exhibited closer stiffness and load-bearing properties to the P structure, although it does not achieve the desired increase in energy absorption due to the presence of G unit cells in the structure.

The last comparison based on the transition type is regarding the structures with diagonal localized morphological transition. Four geometries including G, P, LOCH and LOCV structures were evaluated and compared in Figs. 12 and 13. The LOCH structure reached the first peak load at around 5% strain prior to the plateau area (see Fig. 12**)**. As for the LOCV structure, the stress over the plateau area is higher than LOCH structure since the transition interface, as well as the entire structure, was more resistant to compression. Fig. 13 indicates that the LOCH structure had slightly higher stiffness and yield stress than G and LOCV structures but lower than P structure, while its energy absorption was similar to that of the G structure due to a smooth plateau region observed up to 19% strain. As for the transition morphology in LOCH and LOCV structures, it can be observed that the connection area of

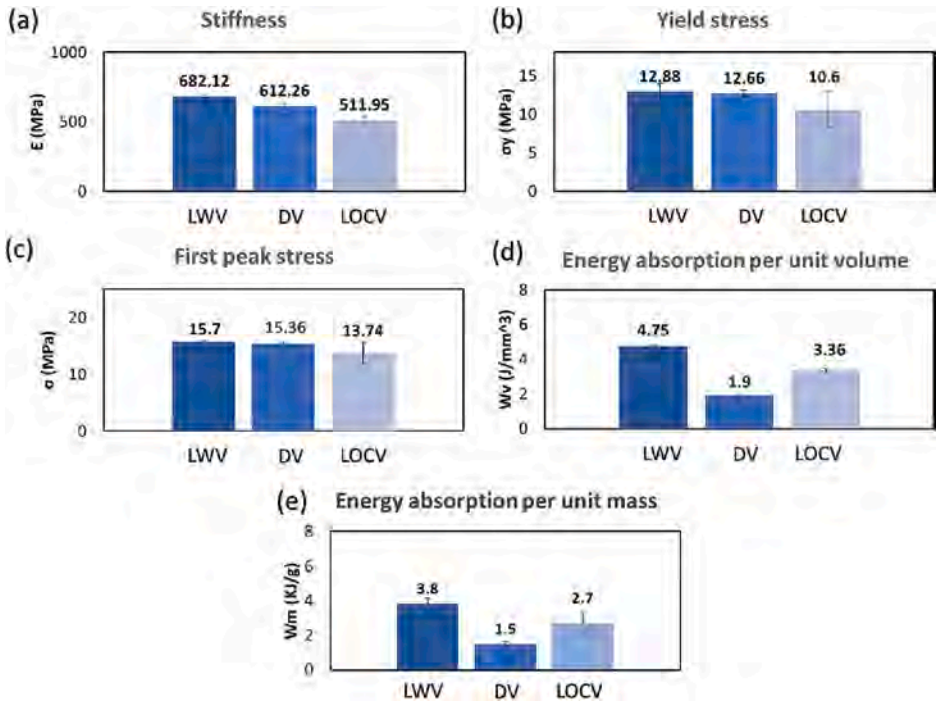

Fig. 17. Bar charts representing a comparison of the mechanical properties of DV, LWV, and LOCV structures: a) Stiffness, b) yield stress, c) first peak stress, d) energy absorption per unit volume, (e) energy absorption per unit.

LOCH was larger than LOCV. In addition, the direction of the interface is oriented by 45 degrees with respect to the loading direction, which indicates that the connection area will play a key role in the mechanical properties. Indeed, in the previous case of LWH and LWV structures, since the direction of the interface was perpendicular to the loading direction, the interface morphology had a less important role in affecting the overall mechanical properties.

Regarding the combination based on the transitions, three geometries including DH, LWH and LOCH structures whose morphological variation occurs with Gyroid horizontal waves on the sample surface were selected and compared. It can be observed that the LOCH and DH structures exhibited a linear elastic zone that reached the yield stress and the first peak stress in a remarkably similar trend as illustrated in Fig. 14 showing minimal difference between the mechanical properties (see Fig. 15**b**). However, the LWH structure showed a higher yield strength as well as a higher energy absorption than the other two structures since the interface transition in this structure was perpendicular to the loading direction instead of being diagonal, as in the other structures. Therefore, it was more resistant to compression so that the plateau region reached at around 28% strain prior to the densification stage. As for the DH structure, the yield stress and energy absorption were slightly lower than the other two structures.

Following the same trend, the last comparison involves structures with contact transition with the vertical waves of the Gyroid unit cells. Therefore, LWV, DV and LOCV structures were selected and compared. As illustrated in Fig. 16, LWV structure showed a similar deformation trend to the G structure with a relatively large and smooth plateau area. However, the curve experienced a slight increase of stress over the plateau area and reached the first densification point at around 28% of strain. In addition, the mechanical properties of LWV structure indicated an energy absorption capacity superior to the other two structures as illustrated in Fig. 17. As for DV and LOCV structures, these were comparable in post-yield stage behavior but differed in the elastic and plateau region. The DV structure exhibited higher stiffness, yield stress as well as peak stress compared to the LOCV structure. Therefore, the DV structure maintained good elastic properties despite entering the densification stage shortly after 10% strain with a significant increase in stress.

3.2. Numerical analysis

Von-Mises stress distributions at different strains ranging from 0 to 30% for the geometries of two uniform structures and four hybrid structures are presented in Fig. 18, including the strain of 0%, 0.5%, 1%, 1.7% (elastic limit), 2.15% (yield stress) and 30%. According to the numerical analyses, the highly stressed regions in the lattice structures were located at the areas joining the unit cells and in the transition area of the hybrid designs. It also can be noticed that the highly stressed regions were enlarged by increasing the applied load on the models.

Specifically, for the G structure illustrated in Fig. 18**(a)**, a concentration of stress was located along the connecting points of the unit cells. This localized stress in the numerical model corresponds to the failure points observed during the experiments, eventually leading to a barreling behavior of the structure. As for the P structure illustrated in Fig. 18**(b)**, the simulation results revealed that this design had the largest stiffness and yield stress compared to the rest of the geometries. In addition, the stress contour in the simulation demonstrated the stress concentration area in the connection zone between the unit cells, which is aligned with the experimental data illustrating similar locations of excessive plastic deformation under compressive loading.

As can be seen in Fig. 18**(c)**, LH structure demonstrated a similar correspondence with the data and deformation behavior of the experimental results compared to the previous two uniform structures. The stress was more concentrated in the interface areas and propagated more on the struts in the Gyroid part of the structure first and then on the entire structure. The Gyroid vertical waves also displayed diagonal shear bands in each unit cell indicating stress concentration. The deviation between the numerical and experimental values in terms of stiffness and yield stress for LWV structure is the lowest among all the compared geometries. According to the numerical analysis, it can be verified that the stress distribution was global so that the deformation started at every joining section of the structure rather than on the unit cells. The numerical results are aligned with the experimental data with the demonstration of the barreling part of the structure, especially for the stress contour of 30% strain, that is the highest strain modelled here. Fig. 18**(e)** demonstrates the propagation of the stress initiated at the

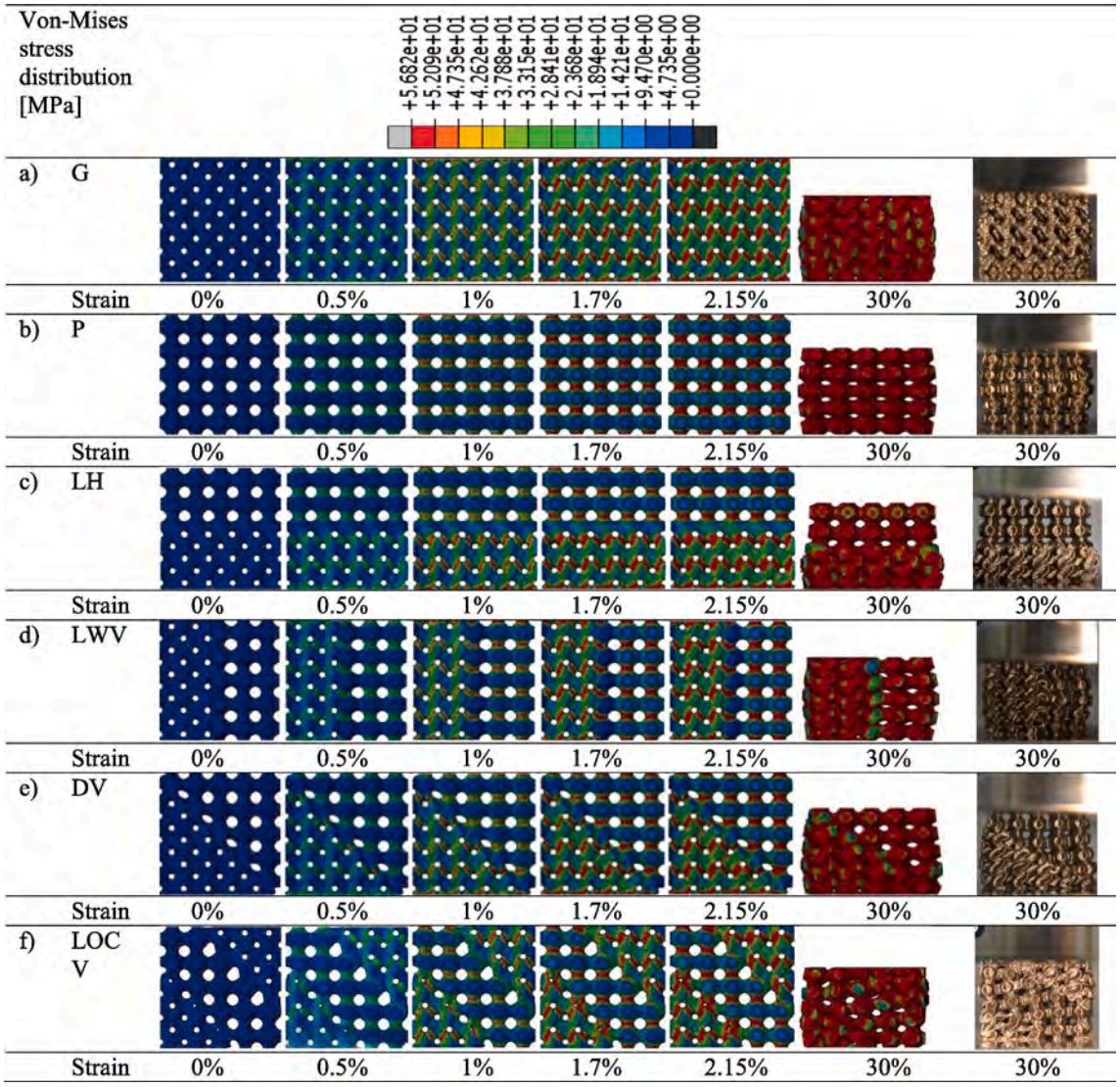

Fig. 18. Von-Mises stress distributions from numerical simulation at various strains compared to the experimental results corresponding to 30% strain for different geometries including (a): G (b) P (c) LH (d) LWV (e) DV and (f) LOCV structure.

diagonal interface at around 0.5% strain and then distributed in both the Gyroid and primitive parts of the structure. When checking higher strains, it can be noticed that the Gyroid part of the structure reached the densification stage prior to the primitive part, which is in agreement with the deformation mechanism observed in the experimental results. As for the LOCV structure, the stress inside the structure was accumulated as well. According to the numerical analysis, the deformation occurred in all struts of the structure approximately uniformly up to 30% strain. In addition, the experimental results revealed that the primitive part in the middle of the structure started to skew because of the uneven morphology and deformation of the Gyroid part from the top and bottom, which is also visible in the numerical results.

3.3. Comparison between experimental and numerical results

Numerical and experimental results were compared in Fig. 19 for the geometries including two uniforms and four hybrid lattice structures. It is worth mentioning that only the results related to the elastic and early plastic deformation stage can be compared with the experimental data based on the parameters of the FE model. According to the results in Fig. 19, the yield strain calculated in numerical analyses is almost identical to the experimental values of approximately 2%, while the yield stress from the simulation is higher than the experimental values except for the LWV structure. The slope of the elastic stage for simulation is slightly higher than the experimental results for all the geometries analyzed. The deviation of the FE analysis concerning the stiffness ranged from 14% to 31.2% while the yield stress showed a difference varying from 3.73% to 20.47%.

The discrepancy between the numerical and the experimental results can be majorly attributed to three factors including possible internal defects, and the high surface roughness of the printed specimens, as well as the definition of material properties in the numerical model. The FE models were based on the perfect designed geometry, while the as-printed specimens demonstrated deviation from the original design, particularly in the case of surface quality as it is a typical issue for AM technologies. Lattice structures fabricated via FDM technology are reported to have several defects including internal voids based on the printing trajectory as well as geometrical deviations [5]. In general, all these defects can influence the mechanical properties. Surface roughness and internal defects can lead to reduced stiffness, especially in structures with relatively thin elements where they can notably change the load bearing section [29]. Therefore, these defects can result in lower stiffness for the as-printed specimen compared to that predicted in the FE simulation for the perfect as-designed geometry. Furthermore, the

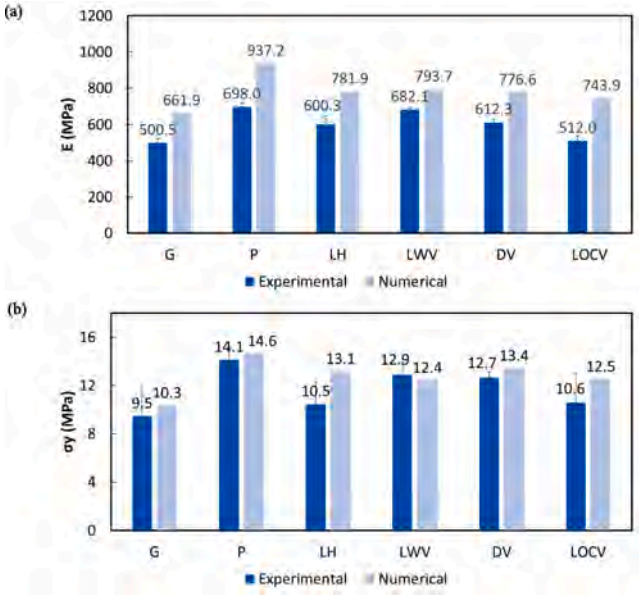

Fig. 19. Comparisons of mechanical properties between numerical simulations and experimental tests for the lattice G, P, LH, LWV, DV and LOCV structures reporting (a) stiffness and (b) Yield stress.

isotropic properties were considered in the constitutive material model in the FE analysis, which can cause some deviation due to the possible anisotropy in material properties induced by the fabrication process via the FDM technique. Overall, although the FE models cannot present the full deformation mechanics, they still provide valuable insight on the stress distribution for the variety of designed geometries.

4. Conclusions

Various lattice structures were designed by using different arrangements of Gyroid and Schwarz primitive TPMS unit cells to study the role of unit cell arrangement on the mechanical response of the integrated lattice structures. Four different transition strategies including uniform, linear transition, diagonal transition, and localized diagonal transition were considered between the two basic unit cells. The mechanical performance of the samples fabricated via the fused deposition modeling technique under quasi-static compressive loading was experimentally analyzed. The following conclusions can be drawn based on the presented experimental observations as well as the numerical simulations:

1) Overall, the experimental results indicated that the topological arrangement of the unit cells had a critical role in determining the mechanical performance of the lattice structures. Specifically, the LWV structures exhibited the best mechanical properties in terms of stiffness, yield stress and energy absorption.
2) The direction of the Gyroid waves (horizontal or vertical) on the sample surface or the stacking strategy was discovered to be important in affecting the mechanical properties of all three different transition strategies (linear, diagonal and localized diagonal). One of the main reasons is attributed to the fact that different interface morphologies were constructed while shifting zero or half of the unit cells of the gyroid part as previously described, which can influence the overall mechanical response under quasi-static compression.
3) It was discovered that there is a high association between the mechanical performance and orientation of the contact interface with respect to the loading direction. The experimental results revealed that the average value of mechanical properties (stiffness, yield stress, first peak stress, energy absorption) tends to be the largest when the orientation of the contact interface with respect to the loading direction is parallel (LWH, LWV) compared to other configurations (DH, DV, LOCH, LOCV). One reason is that structures with different orientations of contact interface than loading direction (non-parallel) experienced shear movement via horizontal direction under compression, which reduced the overall compression resistance of the structures.
4) Finite element models were also developed to evaluate the stress distribution within the lattice structures under different strains as well as to identify the critical sites in each structure. It can be noticed that the numerical results aligned with the experimental observations for the compressive behaviors.
5) Both numerical and experimental data pointed out the criticality of unit cell transition interface design, as the weak point of the hybrid structures. Overall, the obtained results indicated the significant potential of functionally graded designs for the creation of lattice structures with fine-tuned mechanical properties. Further research can also be explored for other potential topological arrangements of lattice structures under different loading conditions.

CRediT authorship contribution statement

Zhuo Xu: Investigation, Formal analysis, Visualization, Writing – original draft. **Irene Lamendola:** Investigation, Software, Formal analysis, Visualization. **Nima Razavi:** Conceptualization, Methodology, Resources, Writing – review & editing, Supervision. **Sara Bagherifard:** Conceptualization, Formal analysis, Methodology, Validation, Resources, Writing – review & editing.

Declaration of Competing Interest

The authors declare that they have no known competing financial interests or personal relationships that could have appeared to influence the work reported in this paper.

Data availability

Data will be made available on request.

Appendix

See Figs. A1-A3 and Table A1-A9.

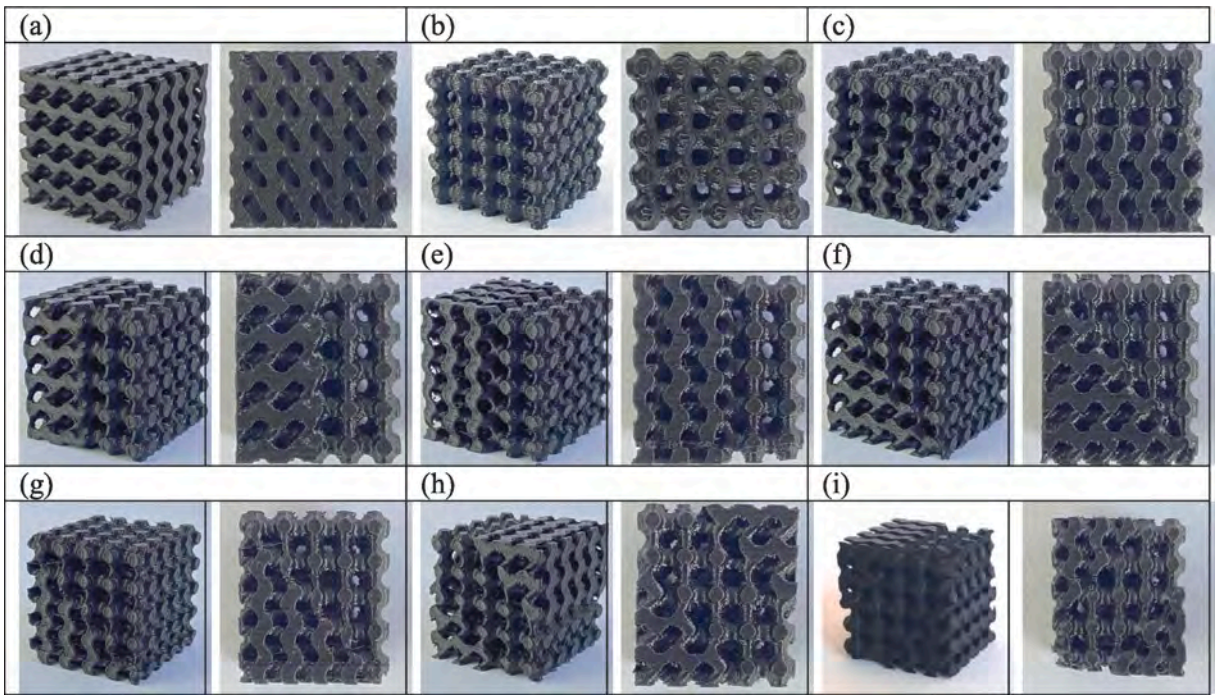

Fig. A1. Iso-view and sideview of (a) G, (b) P, (c) LH, (d) LWH, (e) LWV, (f) DH, (g) DV, (h) LOCH, (i) LOCV.

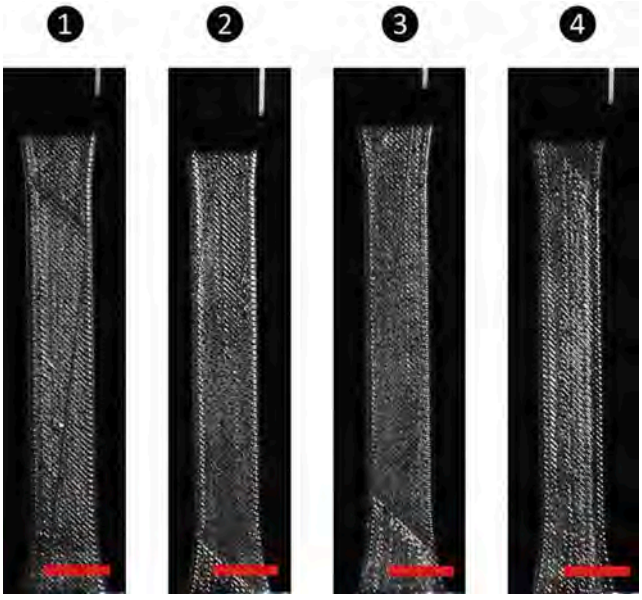

Fig. A2. As-printed four standard dog-bone speicmens (scale bar = 13 mm).

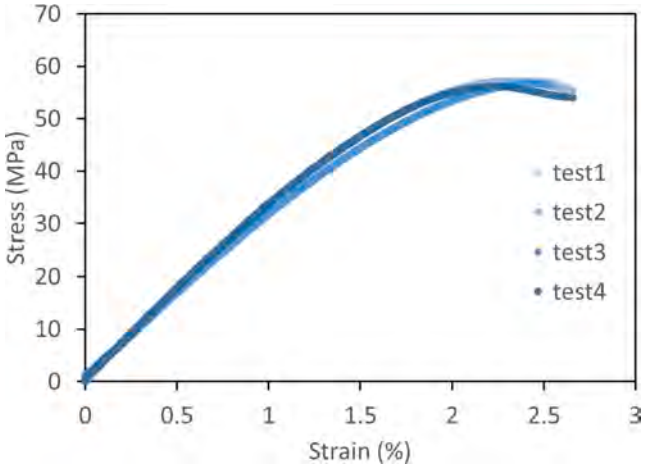

Fig. A3. Stress–strain curves of tensile tests on four standard dog-bone specimens.

Table A1
Raw data for uniform gyroid (G).

G	Test1	Test2	Test3
E [MPa]	502.5	520.66	478.25
Yield Stress [MPa]	8.9	12.13	7.36
FPS [MPa]	13.5	14.83	13.91
Wv [J/mm^3]	3.1	2.5	3.2
Wm[KJ/g]	2.5	2.0	2.6

Table A2
Raw data for uniform primitive (P).

P	Test1	Test2	Test3
E [MPa]	694.55	680.75	718.69
Yield Stress [MPa]	13.5	15	13.9
FPS [MPa]	14.44	17.76	17.66
Wv [J/mm^3]	6.3	6.3	6.6
Wm[KJ/g]	5.1	5.1	5.3

Table A3
Raw data gyroid with linear transition along height (LH).

LH	Test1	Test2	Test3
E [MPa]	545.42	627.87	627.53
Yield Stress [MPa]	8.3	11.53	11.53
FPS [MPa]	14.64	15	14.58
Wv [J/mm^3]	1.8	1.5	1.4
Wm[KJ/g]	1.5	1.2	1.1

Table A4
Raw data for gyroid with linear transition along width (LWH).

LWH	Test1	Test2	Test3
E [MPa]	469.37	496.63	587.63
Yield Stress [MPa]	10.81	11.63	11.45
FPS [MPa]	15.6	16	16.1
Wv [J/mm^3]	4.1	4.2	4.1
Wm[KJ/g]	3.3	3.4	3.3

Table A5
Raw data for gyroid with linear transition along width (LWV).

LWV	Test1	Test2
E [MPa]	689.44	674.79
Yield Stress [MPa]	13.63	12.12
FPS [MPa]	15.5	15.9
Wv [J/mm^3]	5	4.5
Wm[KJ/g]	4.0	3.6

Table A6
Raw data for gyroid with diagonal transition (DH).

DH	Test1	Test2	Test3
E [MPa]	536.05	559.75	526.95
Yield Stress [MPa]	10	10.45	11.4
FPS [MPa]	16.85	14.13	14.4
Wv [J/mm^3]	2.1	2.1	2.2
Wm[KJ/g]	1.7	1.7	1.8

Table A7
Raw data for gyroid with diagonal transition (DV).

DV	Test1	Test2	Test3
E [MPa]	617.73	628.53	590.52
Yield Stress [MPa]	13	12.82	12.15
FPS [MPa]	15.75	15.32	15
Wv [J/mm^3]	1.9	1.7	2.0
Wm[KJ/g]	1.5	1.4	1.6

Table A8
Raw data for gyroid with localized diagonal transition (LOCH).

LOCH	Test1	Test2	Test3
E [MPa]	552.37	603.14	491.69
Yield Stress [MPa]	10.38	10.85	20.06
FPS [MPa]	13.56	14.36	13.8
Wv [J/mm^3]	2.4	2.7	2.6
Wm[KJ/g]	1.9	2.2	2.1

Table A9
Raw data for gyroid with localized diagonal transition (LOCV).

LOCV	Test1	Test2	Test3	Test4	Test5
E [MPa]	522.75	555.4	495.95	492.46	493.2
Yield Stress [MPa]	14.7	10.52	9.36	9.68	8.73
FPS [MPa]	16.21	15	13.6	12.22	11.66
Wv [J/mm^3]	4.9	3	2.5	3	3.4
Wm[KJ/g]	4.0	2.4	2.0	2.4	2.7

References

[1] Wang Y, Zhang L, Daynes S, Zhang H, Feih S, Wang MY. Design of graded lattice structure with optimized mesostructures for additive manufacturing. Mater Des 2018;142:114–23. https://doi.org/10.1016/j.matdes.2018.01.011.

[2] Lei H, Li C, Zhang X, Wang P, Zhou H, Zhao Z, et al. Deformation behavior of heterogeneous multi-morphology lattice core hybrid structures. Addit Manuf 2021;37:101674.

[3] Xu H, Farag A, Pasini D. Multilevel hierarchy in bi-material lattices with high specific stiffness and unbounded thermal expansion. Acta Mater 2017;134:155–66. https://doi.org/10.1016/j.actamat.2017.05.059.

[4] Barnes B, Babamiri BB, Demeneghi G, Soltani-Tehrani A, Shamsaei N, Hazeli K. Quasi-static and dynamic behavior of additively manufactured lattice structures with hybrid topologies. Addit Manuf 2021;vol. 48, no. PB:102466. https://doi.org/10.1016/j.addma.2021.102466.

[5] Xu Z, Medori E, Sarasini F, Razavi N. Quasi-static behavior of 3D printed lattice structures of various scales. Proc Struct Integr 2021;33(2019):578–85. https://doi.org/10.1016/j.prostr.2021.10.064.

[6] Xu Z, Razavi N, Ayatollahi MR. *Functionally Graded Lattice Structures: Fabrication Methods, Mechanical Properties, Failure Mechanisms and Applications*. Elsevier Ltd.; 2022.

[7] Chen W, Watts S, Jackson JA, Smith WL, Tortorelli DA, Spadaccini CM. Stiff isotropic lattices beyond the Maxwell criterion. Sci Adv 2019;5(9):1–7. https://doi.org/10.1126/sciadv.aaw1937.

[8] Dallago M, Winiarski B, Zanini F, Carmignato S, Benedetti M. On the effect of geometrical imperfections and defects on the fatigue strength of cellular lattice structures additively manufactured via Selective Laser Melting. Int J Fatigue 2019;124(February):348–60. https://doi.org/10.1016/j.ijfatigue.2019.03.019.

[9] Han C, Li Y, Wang Q, Wen S, Wei Q, Yan C, et al. Continuous functionally graded porous titanium scaffolds manufactured by selective laser melting for bone implants. J Mech Behav Biomed Mater 2018;80:119–27.

[10] Maskery I, Aboulkhair NT, Aremu AO, Tuck CJ, Ashcroft IA, Wildman RD, et al. A mechanical property evaluation of graded density Al-Si10-Mg lattice structures manufactured by selective laser melting. Mater Sci Eng A 2016;670:264–74.

[11] Maskery I, Hussey A, Panesar A, Aremu A, Tuck C, Ashcroft I, et al. An investigation into reinforced and functionally graded lattice structures. J Cell Plast 2017;53(2):151–65.

[12] Teimouri M, Asgari M. Mechanical performance of additively manufactured uniform and graded porous structures based on topology-optimized unit cells. Proc Inst Mech Eng Part C J Mech Eng Sci 2021;235(9):1593–618. https://doi.org/10.1177/0954406220947119.

[13] Loh GH, Pei E, Harrison D, Monzón MD. An overview of functionally graded additive manufacturing. Addit Manuf 2018;23(July):34–44. https://doi.org/10.1016/j.addma.2018.06.023.

[14] Zhang XY, Fang G, Xing LL, Liu W, Zhou J. Effect of porosity variation strategy on the performance of functionally graded Ti-6Al-4V scaffolds for bone tissue engineering. Mater Des 2018;157:523–38. https://doi.org/10.1016/j.matdes.2018.07.064.

[15] Gibson LJ, Ashby MF. Cellular Solids: Structure and Properties. 2nd ed. Cambridge University Press, © 1997. Figure courtesy of Lorna Gibson and Cambridge University Press; 1997. p. 1997.

[16] Mora Sierra DC, Heydari Astaraee A, Guagliano M, Bagherifard S. Numerical Investigation of Ti6Al4V Gradient Lattice Structures with Tailored Mechanical Response. Adv Eng Mater 2022;24(4):2101760.

[17] Pham MS, Liu C, Todd I, Lertthanasarn J. Damage-tolerant architected materials inspired by crystal microstructure. Nature 2019;565(7739):305–11. https://doi.org/10.1038/s41586-018-0850-3.

[18] Alberdi R, Dingreville R, Robbins J, Walsh T, White BC, Jared B, et al. Multi-morphology lattices lead to improved plastic energy absorption. Mater Des 2020; 194:108883.
[19] Xu S, Shen J, Zhou S, Huang X, Xie YM. Design of lattice structures with controlled anisotropy. Mater Des 2016;93:443–7. https://doi.org/10.1016/j.matdes.2016.01.007.
[20] Xu M, Xu Z, Zhang Z, Lei H, Bai Y, Fang D. Mechanical properties and energy absorption capability of AuxHex structure under in-plane compression: Theoretical and experimental studies. Int J Mech Sci 2019;159(May):43–57. https://doi.org/10.1016/j.ijmecsci.2019.05.044.
[21] Alomarah A, Masood SH, Ruan D. Metamaterials with enhanced mechanical properties and tuneable Poisson's ratio. Smart Mater Struct 2022;31(2):025026.
[22] Riaz S, Fatima N, Rasheed A, Riaz M, Anwar F, Khatoon Y. Metabolic engineered biocatalyst: A solution for PLA based problems. Int J Biomater 2018;2018:1–9.
[23] Maskery I, Aboulkhair NT, Aremu AO, Tuck CJ, Ashcroft IA. Compressive failure modes and energy absorption in additively manufactured double gyroid lattices. Addit Manuf 2017;16:24–9. https://doi.org/10.1016/j.addma.2017.04.003.
[24] Liu X, Wada T, Suzuki A, Takata N, Kobashi M, Kato M. Understanding and suppressing shear band formation in strut-based lattice structures manufactured by laser powder bed fusion. Mater Des 2021;199:109416. https://doi.org/10.1016/j.matdes.2020.109416.
[25] Greco L, Buccino F, Xu Z, Vergani L, Berto F, Guagliano M. Design and Analysis of Energy Absorbent Bioinspired Lattice Structures. pp. 1–20.
[26] Maconachie T, Tino R, Lozanovski B, Watson M, Jones A, Pandelidi C, et al. The compressive behaviour of ABS gyroid lattice structures manufactured by fused deposition modelling. Int J Adv Manuf Technol 2020;107(11-12):4449–67.
[27] Materials P, Materials EI. Standard Test Method for Tensile Properties of Plastics 1. doi: 10.1520/D0638-14.1.
[28] CAE User. Abaqus theory manual. *Abaqus 6.13 Doc.*, no. Dassault Systemes Simulia Corp., Providence, RI, USA; 2014.
[29] Jiang P, Rifat M, Basu S. Impact of surface roughness and porosity on lattice structures fabricated by additive manufacturing- A computational study. Procedia Manuf 2020;48:781–9. https://doi.org/10.1016/j.promfg.2020.05.114.